J. Fluid Mech. (2001), *vol.* 431, *pp.* 135–159. Printed in the United Kingdom

Slow flow of a Bingham fluid in a shallow channel of finite width

By CHIANG C. MEI AND MASATOSHI YUHI†

Department of Civil and Environmental Engineering, Massachusetts Institute of Technology, Cambridge, MA 02139, USA

(Received 14 March 2000 and in revised form 19 September 2000)

We present a theory for the three-dimensional flow of a Bingham-plastic fluid in a shallow and wide channel. Focusing attention on slow flows appropriate for gentle slopes, low discharge rates or the final stage of deposition, we ignore inertia and apply the long-wave approximation. For steady flows, the velocity distribution, total discharge, and section-averaged flux are obtained analytically in terms of the fluid property and the geometry of the channel cross-section. Nonlinear stationary waves, which connect a uniform depth upstream to another uniform depth downstream, are then investigated, for both wet and dry beds. A numerical scheme is applied to calculate the transient flow evolution. The final development of the stationary wave due to steady discharge upstream is obtained numerically and the relation between the tongue-like shape of the wave front and the fluid property is discussed. The phase speed of the stationary wave is also derived analytically. Finally, the transient spreading of a finite fluid mass released from a reservoir after a dam break is simulated numerically. The transient development of the front and the final extent of deposition are examined.

1. Introduction

Many regions in the world are plagued by mud flows which can be triggered by torrential rains, mountain slides or volcanic eruptions. In 1985, the volcanic lahar from Mount Nevado del Ruiz in Colombia was mixed with mountain snow and ice, and resulted in mud flows which took the life of 23 000 inhabitants in the town of Armero (McDowell & Raymer 1986; Mileti *et al.* 1991). More recently mud hazards caused by Hurricane Mitch led to thousands of human deaths, and damaged half of the nation's infrastructure in Honduras alone. The 1991 eruption of Mt. Pinatubo in Phillipines released roughly one cubic mile of volcanic ash and rock fragments covering the adjacent mountain slopes (Newhall & Punongbayan 1996). Heavy rainfall following the fallout led to gigantic mud floods which damaged thousands of villages.

Mud is one of several forms of natural debris and is distinguished by the abundance of small and cohesive solid grains and the high water content. Rheologically the most characteristic feature of mud is its plastic-like behaviour. In particular the shear stress must exceed the yield stress, τ_0, before flow begins. For understanding the hydrodynammics of muddy rivers, numerous experiments for unidirectional shear flows (e.g. Qian *et al.* 1985; Wang & Qian 1985) have shown that, when the clay concentration exceeds just a few percent by volume, the stress–strain relation is closely

† Permanent address: Department of Civil Engineering, Kanazawa University, Kanazawa, Ishikawa, 920-8667, Japan.

approximated by the Bingham law, which can be generalized for three-dimensional flows as follows (see e.g. Prager 1961)

$$\epsilon_{ij} = 0 \quad \text{if } \tau \leqslant \tau_0 \tag{1.1}$$

and

$$\tau_{ij} = \left(\mu + \frac{\tau_0}{\epsilon}\right) \epsilon_{ij} \quad \text{if } \tau \geqslant \tau_0 \tag{1.2}$$

where

$$\tau = (\tfrac{1}{2}\tau_{ij}\tau_{ij})^{1/2} \quad \text{and} \quad \epsilon = (\tfrac{1}{2}\epsilon_{ij}\epsilon_{ij})^{1/2} \tag{1.3}$$

where τ_{ij} and ϵ_{ij} are the stress tensor and the rate-of-strain tensor, respectively. For many types of muds, both the yield stress and the Bingham viscosity are empirical functions of the volume concentration of clay minerals and possibly the pH values and salinity (see e.g. Krone 1963; Migniot 1968; Allersma 1980). To cover a broader range of shearing rates for mud as well as other industrial materials such as foams, gels and emulsions, the Herschel–Bulkley model which combines the yield stress and power-law dependence has also been proposed.

Because of the nonlinear constitutive relation, early analytical studies of Bingham fluids are limited largely to steady unidirectional flows in closed conduits (Bird, Dai & Yarusso 1983). For steady uniform flows in open channels of finite width, Johnson (1970) has given solutions for a steady inclined channels of various cross-sections (see also Johnson & Rodine 1984). Using the Herschel–Bulkley model, Coussot (1997) has proposed an empirical formula for the discharge in an open channel of rectangular and trapezoidal cross-section. A shape parameter is introduced to account for the geometrical characteristics of the channel. The specific form of this parameter must be found empirically for each cross-sectional shape. The results obtained from his formulae differ from experimental measurements by about 30–35%. Non-uniform and steady flows in long vessels have been studied recently by Wilson & Taylor (1996) and Taylor & Wilson (1997).

For unsteady flows with a free surface, as in natural streams, Liu & Mei (1989) studied unidirectional long waves in shallow layers over a flat bed of infinite width. Assuming slow flows, they used the lubrication approximation and examined a variety of transient phenomena including stationary waves, the transient release and final deposition of mud piles. Good agreement with experiments has been found in the wave speed and the surface profile of a mud current flowing down a dry bed, almost up to the tip where the flow depth is zero and the local slope is large. Extensions to the Herschel–Bulkley model have been made by Huang & Garcia (1998). For radially symmetric flows, Balmforth *et al.* (2000) have also used the Herschel–Bulkley model to derive analytical and numerical solutions for the evolution of isothermal lava domes on a horizontal plane. Justification of the long-wave lubrication approximation by perturbation analysis has been given by Liu & Mei (1990) and by Balmforth & Craster (1999). Local refinement for the small neighbourhood of the steep wave front has been investigated by Piau (1996). In high-speed flows, roll waves, which are periodic hydraulic jumps in clear water, appear also in laminar flows of Bingham and power-law fluids. Accounting for nonlinear convective inertia, Liu & Mei (1994) have treated the boundary layer equations by the momentum integral approximation. Guided by a linearized instability theory they have performed numerical computations to predict the nonlinear formation of roll waves. A more analytical theory of periodic shocks has been advanced by Ng & Mei (1994) for a power-law fluid.

For three-dimensional flows, the long-wave approximation has been applied to the

slow and steady spreading of mud released from a point source on an inclined plane, by Hulme (1974) using the Bingham model, and by Coussot & Proust (1996) and Wilson & Burgess (1996) using the Herschel–Bulkley model. Coussot, Proust & Ancey (1996) have also studied the static problem of the final shape of a mud pile at rest on an inclined plane. However, they introduced a physically questionable approximation that all free surface contours are parallel.

A review of numerical methods for non-Newtonian fluids without a free surface can be found in Crochet & Walters (1983) and Crochet, Davies & Walters (1984). For viscoelastic flows with free surfaces several computational schemes have been developed in the last decade (e.g. Keunings 1990; Sato & Richardson 1994; Mao & Khayat 1995; Petra & Nassehi 1996).

In this paper we extend the approximate theory of Liu & Mei (1989) from two to three dimensions for a thin layer of Bingham fluid flowing down an open channel of finite width. The main assumptions are: (i) homogeneous fluid, (ii) negligible inertia, (iii) very small depth-to wavelength ratio, and (iv) finite ratio of wave amplitude to depth. Steady uniform flows are first discussed. Next, stationary waves which propagate at a constant speed are investigated for both wet and dry beds. The front of a stationary wave is studied numerically and the relation between fluid property and the typical tongue-like shape at the wave front is examined. The phase speed of the stationary wave is derived analytically. Finally, the transient spreading of a finite fluid volume released from a reservoir due to the breaking of a dam is calculated numerically. The effect of the fluid property and the channel shape on the extent of final spreading is investigated.

Rapid flows, important to mud floods in mountain streams and volcano eruptions, are left for future studies.

2. Lubrication approximation for long waves

Consider a three-dimensional laminar flow of a thin layer of mud flowing down an inclined wide channel. Let the typical fluid depth and wavelength be D and L respectively. We shall assume that

$$D/L \ll 1, \tag{2.1}$$

i.e. long waves. Let u and μ be the typical flow speed and kinematic viscosity respectively. The Reynolds number defined by $Re = \rho u D^2/\mu L$ and the Froude number defined by $Fr = u^2/gD$ (g is gravitational acceleration) are taken to be of the order D/L at most and small.

We consider a straight channel whose cross-section is symmetric with respect to the centreplane ($y = 0$), as shown in figure 1. The x-axis coincides with the longitudinal axis along the channel bottom, and is inclined at the angle θ with respect to the horizon. The y-axis is in the transverse direction and the z-axis is perpendicular to both the x- and y-axes. The free surface and the channel bottom are described by $z = h(x, y, t)$ and $z = H(y)$, respectively. Mass conservation requires that

$$\frac{\partial h}{\partial t} + \frac{\partial q_x}{\partial x} + \frac{\partial q_y}{\partial y} = 0 \tag{2.2}$$

where (q_x, q_y) denote the depth-integrated flux in (x, y)-directions. By invoking the lubrication approximation, the inertia is negligible and pressure is hydrostatic.

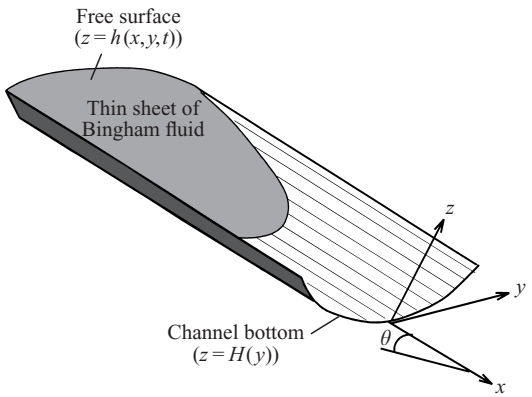

FIGURE 1. Definition sketch.

For vanishing shear stresses on the free surface it is easy to show that

$$\tau_{xz} = \rho g \left(\sin\theta - \cos\theta \frac{\partial h}{\partial x} \right) (h - z), \tag{2.3a}$$

$$\tau_{yz} = \rho g \left(-\cos\theta \frac{\partial h}{\partial y} \right) (h - z). \tag{2.3b}$$

Let us define the total shear stress by

$$\tau(x, y, z, t) = \left(\tau_{xz}^2 + \tau_{yz}^2 \right)^{1/2}. \tag{2.4}$$

At the channel bed $z = H(y)$ the total shear stress τ_b is

$$\tau_b = \rho g (h - H) \left[\left(\sin\theta - \cos\theta \frac{\partial h}{\partial x} \right)^2 + \left(-\cos\theta \frac{\partial h}{\partial y} \right)^2 \right]^{1/2}. \tag{2.5}$$

If $\tau_b > \tau_0$, fluid motion is possible with $(u, v) \neq 0$. In particular there is shear below the yield surface ($H < z < h_0$) defined by

$$\tau = (x, y, h_0(x, y, t), t) = \tau_0, \tag{2.6}$$

which amounts to a relation between the free surface height h and the yield surface height $h_0(x, y, t)$

$$\rho g (h - h_0) \left[\left(\sin\theta - \cos\theta \frac{\partial h}{\partial x} \right)^2 + \left(-\cos\theta \frac{\partial h}{\partial y} \right)^2 \right]^{1/2} = \tau_0. \tag{2.7}$$

Since there can be no slip on the bed, and no shear on the yield surface,

$$u = v = 0 \quad \text{on } z = H, \qquad \frac{\partial u}{\partial z} = \frac{\partial v}{\partial z} = 0 \quad \text{on } z = h_0, \tag{2.8}$$

the velocity components beneath the yield surface must be

$$u(x, y, z, t) = \frac{\rho g}{2\mu} \left(\sin\theta - \cos\theta \frac{\partial h}{\partial x} \right) \left[(h_0 - H)^2 - (z - h_0)^2 \right], \quad H < z < h_0, \tag{2.9a}$$

$$v(x, y, z, t) = \frac{\rho g}{2\mu} \left(-\cos\theta \frac{\partial h}{\partial y} \right) \left[(h_0 - H)^2 - (z - h_0)^2 \right], \quad H < z < h_0. \tag{2.9b}$$

Above the yield surface there is no velocity shear. A 'plug flow' exists:

$$u_p(x,y,t) = \frac{\rho g}{2\mu}\left(\sin\theta - \cos\theta\frac{\partial h}{\partial x}\right)(h_0 - H)^2, \quad h_0 < z < h, \tag{2.10a}$$

$$v_p(x,y,t) = \frac{\rho g}{2\mu}\left(-\cos\theta\frac{\partial h}{\partial y}\right)(h_0 - H)^2, \quad h_0 < z < h. \tag{2.10b}$$

If $\tau_b < \tau_0$, then $h_0 = H(y)$ and there is no flow at all.

Now the depth-integrated fluxes can be calculated as

$$q_x = \int_H^{h_0} u\,\mathrm{d}z + (h - h_0)u_p, \quad q_y = \int_H^{h_0} v\,\mathrm{d}z + (h - h_0)v_p \tag{2.11}$$

to yield the depth-integrated law of mass conservation

$$\frac{\partial h}{\partial t} + \frac{\rho g}{\mu}\frac{\partial}{\partial x}\left[\left(\sin\theta - \cos\theta\frac{\partial h}{\partial x}\right)F\right] + \frac{\rho g}{\mu}\frac{\partial}{\partial y}\left[\left(-\cos\theta\frac{\partial h}{\partial y}\right)F\right] = 0 \tag{2.12}$$

where

$$F(h, h_0, H) = \tfrac{1}{6}(3h - h_0 - 2H)(h_0 - H)^2. \tag{2.13}$$

If h_0 is eliminated from (2.13) with the help of (2.7), (2.12) becomes a nonlinear diffusion equation for h, which holds only wherever there is flow, i.e. where $\tau_b > \tau_0$. The one-dimensional limit (where $\partial/\partial y = 0$) of this equation has been used by Liu & Mei (1989) in several theoretical studies, and has been confirmed for stationary waves flowing down a dry bed for a water–kaolinite mixture. In the special limit of a flat bed, the two-dimensional extension has been derived by an asymptotic analysis (Balmforth & Craster 1999).

We now introduce the following dimensionless variables:

$$(x, y) = D\cot\theta(x', y'), \quad (z, h, h_0, H) = D(z', h', h_0', H'), \tag{2.14a}$$

$$t = \frac{\mu\cos\theta}{\rho g D\sin^2\theta}t', \tag{2.14b}$$

$$(u, v, u_p, v_p) = \frac{\rho g D^2\sin\theta}{\mu}(u', v', u_p', v_p'), \tag{2.14c}$$

$$(q_x, q_y) = \frac{\rho g D^3\sin\theta}{\mu}(q_x', q_y'), \tag{2.14d}$$

$$F = D^3F', \quad Q = \frac{\rho g D^4\cos\theta}{\mu}Q', \tag{2.14e}$$

where D is the characteristic length scale in the z-direction such as the total fluid depth at the inlet boundary, and Q denotes the total discharge over the channel cross-section. In view of the long-wave assumption, the normalization defined by (2.14*a*) is meaningful only for a small bed slope.

The normalized velocity components and the law of mass conservation follow easily from (2.9), (2.10) and (2.12). Specifically one simply replaces the factors $\rho g/\mu, \sin\theta$ and $\cos\theta$ by unity. For later convenience we record the normalized version of (2.12)

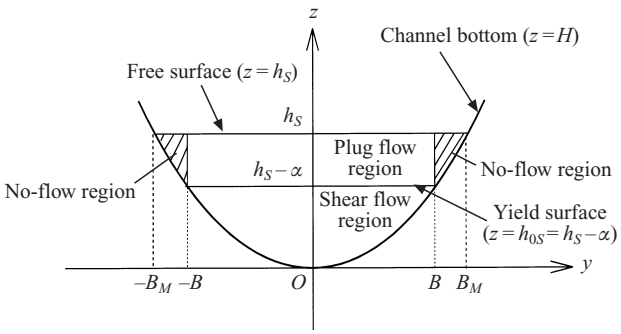

FIGURE 2. Cross-section of a steady uniform flow.

after dropping the primes,

$$\frac{\partial h}{\partial t} + \frac{\partial}{\partial x}\left[\left(1 - \frac{\partial h}{\partial x}\right)F\right] + \frac{\partial}{\partial y}\left[-\frac{\partial h}{\partial y}F\right] = 0, \tag{2.15}$$

while (2.13) is unchanged. The yield surface, $z = h_0$, is related to h through

$$(h - h_0)\left[\left(1 - \frac{\partial h}{\partial x}\right)^2 + \left(-\frac{\partial h}{\partial y}\right)^2\right]^{1/2} = \frac{h_c}{D} \equiv \alpha \tag{2.16}$$

where h_c is the threshold depth of a uniform layer of mud about to flow down an inclined plane of slope θ

$$h_c = \frac{\tau_0}{\rho g \sin\theta}. \tag{2.17}$$

The parameter α is the ratio between the critical depth h_c and the characteristic depth D

$$\alpha = \frac{h_c}{D} = \frac{\tau_0}{\rho g D \sin\theta} \tag{2.18}$$

which also represents the ratio of the yield stress to the bottom shear stress of a uniform flow of depth D, hence is a measure of plasticity. The Newtonian limit corresponds to $\alpha = 0$. For a uniform flow to exist, it is necessary that $h > \alpha$.

The non-dimensional form of the constraint, $\tau_b > \tau_0$, is

$$(h - H)\left[\left(1 - \frac{\partial h}{\partial x}\right)^2 + \left(-\frac{\partial h}{\partial y}\right)^2\right]^{1/2} > \alpha. \tag{2.19}$$

3. Steady uniform flow

When the flow is steady and uniform along the x-direction, i.e. $\partial/\partial t = \partial/\partial x = 0$, h and h_0 must then be independent of y as seen from (2.15). That is, $h = h_S$ and $h_0 = h_{0S}$ are constants everywhere in the flow region. The flow is then confined in an effective width $2B$ (figure 2) whose value can be determined from (2.16) by requiring that

$$h_{0S} = H_B \equiv H(\pm B) = h_S - \alpha. \tag{3.1}$$

For a given $H(y)$ and α, the flow half-width B is less than the maximum half-width B_M of the channel. This result is of course not surprising since the bed stress is too weak for $|y| > B$ where the mud depth is too small. Under the present approximation,

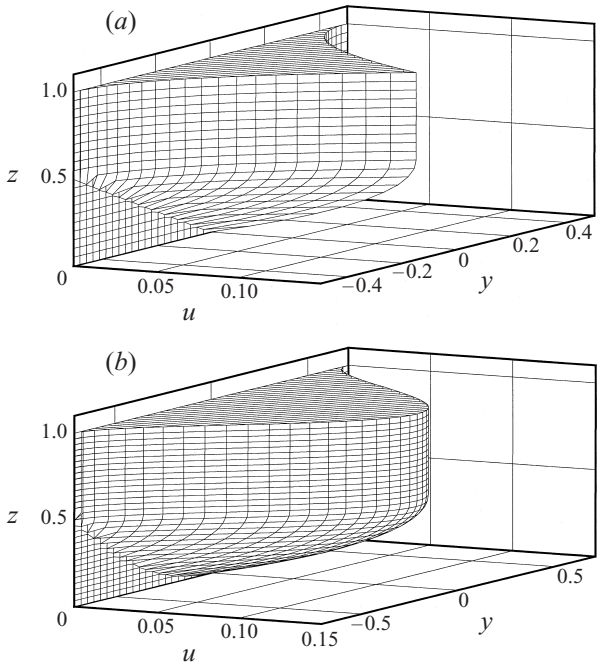

FIGURE 3. Velocity distribution in channels of power-law cross-section $H = m|y|^n$ ($m = 1$, $\alpha = 0.5, h_S = 1$). The yield surface is located at $z = h_{0S} = 0.5$. (*a*) $n = 1$ (triangular channel), (*b*) $n = 2$ (parabolic channel).

the free surface of the non-moving mud between the flow region and the channel banks can in principle be anything, as long as the bed shear stress is below the yield stress. We shall assume for simplicity that the transverse uniformity extends to the channel banks so that $h = h_S$ up to $|y| = B_M$ where $h_S = H(B_M)$.

The longitudinal velocities in the shear flow and plug flow zones are given by (2.9*a*) and (2.10*a*) respectively with $\partial h/\partial x = 0$ and $h \to h_S$ and $h_0 \to h_{0S}$. This profile is formally identical to the two-dimensional steady uniform flow on a plane bed of the same local depth (Liu & Mei 1989). The transverse velocity $v = v_p = 0$ vanishes everywhere.

The flux is then calculated to be

$$q_x = \tfrac{1}{6}(3h_S - h_{0S} - 2H)(h_{0S} - H)^2 = \tfrac{1}{6}(2h_S + \alpha - 2H)(h_S - \alpha - H)^2. \tag{3.2}$$

It is shown in Appendix A that the steady uniform flow is stable to all small wave-like disturbances.

For a prescribed total discharge Q, conservation of mass requires

$$Q = \tfrac{1}{3}\int_0^B (2h_S + \alpha - 2H)(h_S - \alpha - H)^2 \mathrm{d}y. \tag{3.3}$$

We present below numerical results for a channel with a polynomial cross-section:

$$H = m|y|^n. \tag{3.4}$$

The parameter m is a measure of the bank steepness, with $m = 0$ corresponding to a flat bed of infinite width. The power n represents the channel smoothness at the centreline. First, we plot in figure 3 the typical velocity profiles for the special cases

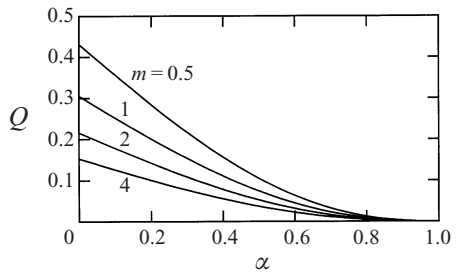

FIGURE 4. Total discharge Q in parabolic channels as a function of α and m.

of $n = 1$ and 2, corresponding to triangular and parabolic cross-sections respectively. Because of the normalization, all vertical scales are much exaggerated in comparison with the horizontal scales. The plug and shear flow regions are clearly seen above and beneath the yield surface respectively. The longitudinal velocity takes its maximum on the centreplane. For a triangular channel with $n = 1$, the velocity distribution is sharply peaked along the axis $y = 0$ due to the discontinuous change of the bottom slope. Note that the horizontal shear rate $\partial u/\partial y = O(D/L) \ll 1$ and the corresponding shear stress is very small, $\tau_{xy} = O(D/L)^2$. The component τ_{xz} dominates the total stress in (2.4) and defines the plug zone. The half-width of the flow region, B, is determined from (3.1),

$$B = \left(\frac{h_S - \alpha}{m}\right)^{1/n}. \tag{3.5}$$

It can also be shown that

$$\begin{aligned} Q &= \frac{4n^3m^3}{(n+1)(2n+1)(3n+1)}B^{3n+1} + \frac{2n^2m^2\alpha}{(n+1)(2n+1)}B^{2n+1} \\ &= \frac{4n^3(h_S-\alpha)^3}{(n+1)(2n+1)(3n+1)}\left(\frac{h_S-\alpha}{m}\right)^{1/n} + \frac{2n^2(h_S-\alpha)^2\alpha}{(n+1)(2n+1)}\left(\frac{h_S-\alpha}{m}\right)^{1/n}. \end{aligned} \tag{3.6}$$

The total discharge Q in parabolic channels ($n = 2$) is plotted as a function of α and m in figure 4. As the Bingham parameter α decreases, the value of Q increases. It is also seen that Q is larger for smaller m, i.e. a wider channel. From (3.6), the section-averaged flux, $\langle q_x \rangle$ is

$$\langle q_x \rangle = \frac{Q}{2B} = \frac{2n^3(h_S-\alpha)^3}{(n+1)(2n+1)(3n+1)} + \frac{n^2(h_S-\alpha)^2\alpha}{(n+1)(2n+1)}. \tag{3.7}$$

Note that the section-averaged flux is a function of α and n but is independent of m.

In the limit of $m = 0$ and finite n, $H = 0$ for all y; the flow is strictly two-dimensional with the velocity being uniform for all y. On the other hand, in the limit of finite m but $n \to \infty$, the bed is flat for all $|y| < 1$ and the dimensionless flow width approaches unity according to (3.5). For $|y| > 1$ H becomes unbounded, implying a rectangular channel with vertical walls along $y = \pm 1$. Within the channel the velocity is uniform in y for $|y| < 1$ only, hence is two-dimensional but non-zero along the effective sidewalls. This discontinuity is a shortcoming of the power-law model for the channel which is incompatible with the long-wave approximation near $|y| = 1$.

Results for a semi-elliptic cross-section are given in Appendix B.

4. Numerical scheme for transient motion

To solve transient problems we have developed a numerical scheme based on the finite volume approach. For spatial discretization a staggered mesh system is introduced, in which h is evaluated at the cell centre (i, j), and the fluxes q_x and q_y are evaluated at cell interfaces, $(i \pm 1/2, j)$ and $(i, j \pm 1/2)$, respectively. All spatial derivatives are approximated by second-order central differences. Employing the ADI (alternating direction implicit) scheme (Douglas 1955; Peaceman & Rachford 1955), we discretize in time so that the truncation error is $O(\Delta t)^2$.

Computations are carried out on a fixed grid, while the free boundary of the flow region is moving in general. This means that the instantaneous location of the free boundary must be tracked in the course of computations. In order to distinguish the flow and no-flow regions, we first check the constraint condition (2.19) at each cell interface. In the flow region where (2.19) is satisfied, the fluxes are approximated by

$$q^{n+1/2}_{x,i+1/2,j} = F^n_{i+1/2,j}\left(1 - \frac{h^{n+1/2}_{i+1,j} - h^{n+1/2}_{i,j}}{\Delta x}\right), \quad q^{n+1}_{y,i,j+1/2} = F^{n+1/2}_{i,j+1/2}\left(-\frac{h^{n+1}_{i,j+1} - h^{n+1}_{i,j}}{\Delta y}\right). \tag{4.1}$$

Note that the fluxes q_x and q_y are linearized with respect to $h^{n+1/2}_{i,j}$ or $h^{n+1}_{i,j}$. In order to evaluate the value of F at the cell interface, the free surface height at cell interfaces is first determined by averaging the values at adjacent grid points: $h_{i+1/2,j} = h_{i,j} + h_{i+1,j}/2$ and $h_{i,j+1/2} = h_{i,j} + h_{i,j+1}/2$. In summary, (2.15) is discretized to the following tridiagonal form:

$$\begin{aligned} &-\frac{F^n_{i-1/2,j}}{(\Delta x)^2}\,h^{n+1/2}_{i-1,j} + \left[\frac{2}{\Delta t} + \frac{F^n_{i-1/2,j} + F^n_{i+1/2,j}}{(\Delta x)^2}\right] h^{n+1/2}_{i,j} - \frac{F^n_{i+1/2,j}}{(\Delta x)^2} h^{n+1/2}_{i+1,j} \\ &= \frac{2}{\Delta t} h^n_{i,j} - \frac{F^n_{i+1/2,j} - F^n_{i-1/2,j}}{\Delta x} \\ &\quad + \frac{F^n_{i,j-1/2}\,h^n_{i,j-1} - (F^n_{i,j-1/2} + F^n_{i,j+1/2})h^n_{i,j} + F^n_{i,j+1/2}\,h^n_{i,j+1}}{(\Delta y)^2}, \end{aligned} \tag{4.2a}$$

$$\begin{aligned} &-\frac{F^{n+1/2}_{i,j-1/2}}{(\Delta y)^2}\,h^{n+1}_{i,j-1} + \left[\frac{2}{\Delta t} + \frac{F^{n+1/2}_{i,j-1/2} + F^{n+1/2}_{i,j+1/2}}{(\Delta y)^2}\right] h^{n+1}_{i,j} - \frac{F^{n+1/2}_{i,j+1/2}}{(\Delta y)^2}\,h^{n+1}_{i,j+1} \\ &= \frac{2}{\Delta t} h^{n+1/2}_{i,j} - \frac{F^{n+1/2}_{i+1/2,j} - F^{n+1/2}_{i-1/2,j}}{\Delta x} \\ &\quad + \frac{F^{n+1/2}_{i-1/2,j}\,h^{n+1/2}_{i-1,j} - (F^{n+1/2}_{i-1/2,j} + F^{n+1/2}_{i+1/2,j})h^{n+1/2}_{i,j} + F^{n+1/2}_{i+1/2,j}\,h^{n+1/2}_{i+1,j}}{(\Delta x)^2}. \end{aligned} \tag{4.2b}$$

At each time step, the inequality (2.19) is checked to determine the free boundary and equation (4.2) is then solved to the next time step.

As a validation of the numerical scheme, calculations have been carried out for a long-crested permanent wave advancing down a dry inclined plane. At the upstream boundary the normalized free surface height is taken to be unity for all time, $h_-(0, t) = 1$. With the grid sizes $\Delta x = 0.02$ and $\Delta t = 0.001$ the computed free surface

profile compares very well with the analytical and measured results by Liu & Mei (1989).

5. Stationary waves

Consider a straight channel initially filled with mud with the centreline depth h_+. From $t = 0$, additional mud is introduced steadily at some station far upstream. After a long time a stationary (permanent) wave front is formed which propagates down the channel at a constant speed C. The objectives here are to predict the geometry of the wave front and the wave speed, as functions of the Bingham parameter α, the channel geometry and the downstream state.

Two initial states which are also the asymptotic uniform states far downstream are of interest. In the first, the mud is sufficiently deep ($h_+ > \alpha$) so that there is flow before fresh mud enters. In the second the mud is everywhere too shallow ($h_+ < \alpha$) so that there is no flow, with the dry bed $h_+ = 0$ being a special limit. In either case, the half-width B_{M+} of the mud-filled region in a power-law channel is given by

$$B_{M+} = \left(\frac{h_+}{m}\right)^{1/n} \tag{5.1}$$

under the assumption of extended transverse uniformity.

After a long enough time a uniform state is also expected far upstream, where the free surface height is denoted by h_-. The upstream yield surface height is $h_{0-} = h_- - \alpha$. Two types of flow will be distinguished according to whether the downstream surface is lower or higher than the upstream yield surface. We shall refer to case (*a*) if $h_+ < h_- - \alpha$ corresponding to a high influx rate, and case (*b*) if $h_+ > h_- - \alpha$ corresponding to a low influx rate. These are summarized in figure 5.

5.1. *Shape of the stationary wave front*

In principle the permanent wave profile can be found by introducing the moving coordinate $\xi = x - Ct$ and assuming $h = h(\xi, y)$ and $h_0 = h_0(\xi, y)$. Equation (2.15) can then be rewritten as a partial differential equation for h,

$$\frac{\partial}{\partial \xi}(-Ch + q_x) + \frac{\partial q_y}{\partial y} = 0 \tag{5.2}$$

which is no less difficult to solve than the full transient problem because of the nonlinearity and the unknown position of the wave edge. We therefore choose to solve (2.15) numerically as an initial-value problem under the constraint of (2.19). The stationary waves are then obtained as the final steady state for sufficiently large t.

Calculations have been carried out for $\alpha = 0$ to 0.9; both the wet and dry downstreams are considered. The free surface height h_- at the inlet boundary($x = 0$) is set to unity. Initially the free surface height is set to be h_+ for all $x > 0$. If $h_+ < h_- - \alpha$ (case (*a*), high influx rate), we must have $B_{M+} < B_-$, so the initial condition is

$$h(x, y, t = 0) = h_+, \quad 0 \leqslant y \leqslant B_{M+}. \tag{5.3}$$

On the other hand, if $h_+ > h_- - \alpha$ (case (*b*), low influx rate), then $B_{M+} > B_-$. The initial condition is

$$h(x, y, t = 0) = h_+, \quad 0 \leqslant y \leqslant B_-. \tag{5.4}$$

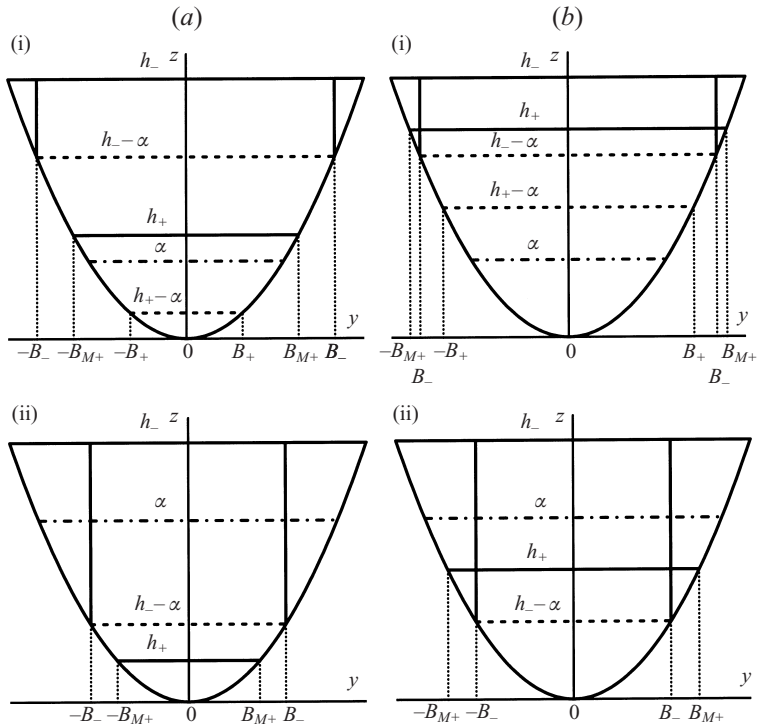

FIGURE 5. Schematic view of the cross-section of the flow at far upstream and downstream. (*a*i) High influx rate $h_+ < h_- - \alpha$ and flowing downstream ($h_+ \geqslant \alpha$), (*a*ii) High influx rate $h_+ < h_- - \alpha$ and stagnant downstream ($h_+ < \alpha$), (*b*i) Low influx rate $h_+ > h_- - \alpha$ and flowing downstream ($h_+ \geqslant \alpha$), (*b*ii) Low influx rate $h_+ > h_- - \alpha$ and stagnant downstream ($h_+ < \alpha$).

For all $t \geqslant 0$ a steady flux is added at the upstream boundary according to (3.2). No transverse flux ($q_y = 0$) is allowed at the side boundary ($y = B_-$), and on the centreplane ($y = 0$). The typical grid size used in the calculations is $\Delta x = 0.02$, $\Delta y = 0.02$, and $\Delta t = 0.001$. In the following numerical results for parabolic channels are presented. Similar investigations have been made for triangular and semi-elliptic channels, with qualitatively the same conclusions.

At the initial stage, the wave propagates much faster than the final steady speed. The wave speed then decreases rapidly until $t \sim 30$ to 50; afterwards it continues to decrease very slowly. Calculations are continued until the flow field reaches the steady state, numerically considered to be when $\mathrm{d}C/\mathrm{d}t < 10^{-4}$. In this study, the final steady states are attained at $t \sim 100$ to 400. The non-dimensional time that is necessary to reach the final state depends mainly on α. As α increases (higher yield stress), this relaxation time increases.

Figures 6 and 7 shows respectively the final free surfaces and yield surfaces for $\alpha = 0.5$ and $m = 1$. Three uniform depths, $h_+ = 0.7$ (flowing), 0.3 (stagnant), and 0 (dry) are taken as the initial state for the downstream. Near the inlet boundary, the flow field becomes uniform after a long time, corresponding to the solutions in § 3. Near the wave front, a tongue-like front can be seen. For the larger h_+ (flowing downstream), the front is more elongated and flatter. For the stagnant and dry downstream, the wave front is steep suggesting local inaccuracy of the long-wave approximation. The yield surface has a rapid transverse variation near the banks.

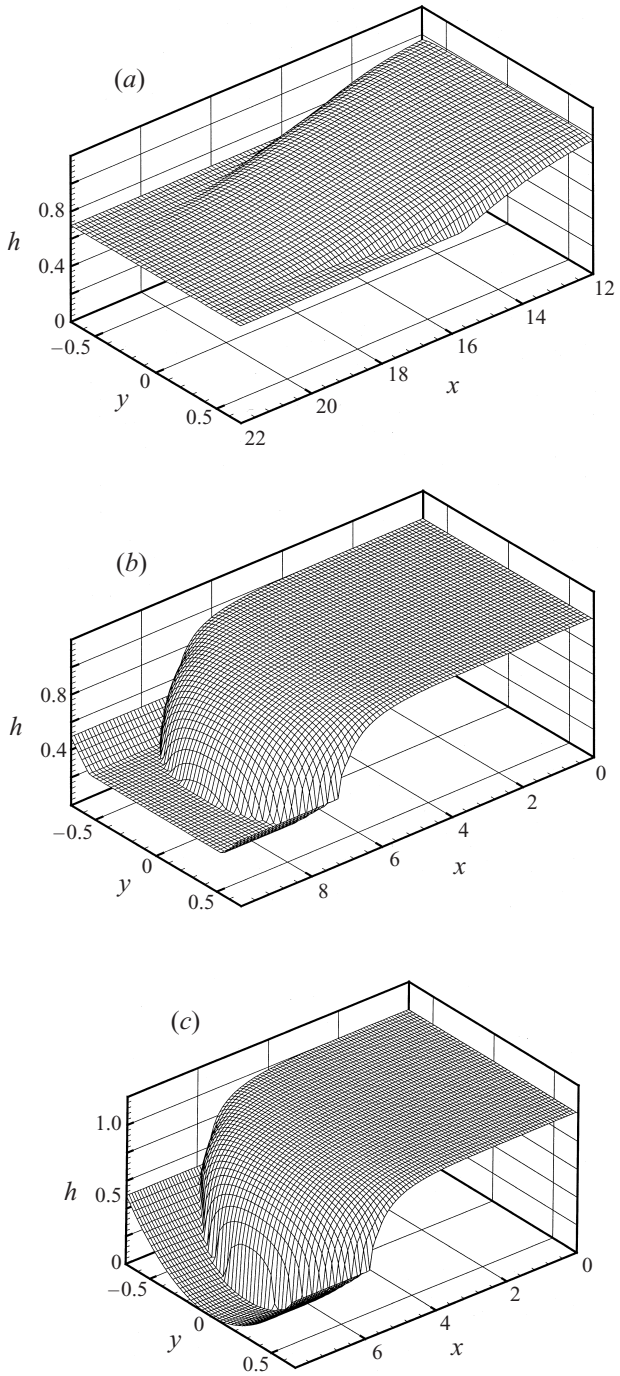

FIGURE 6. Free surface of the wave front in a parabolic channel ($n = 2, m = 1, \alpha = 0.5$): (*a*) flowing downstream ($h_+ = 0.7$), (*b*) stagnant downstream ($h_+ = 0.3$), (*c*) dry downstream ($h_+ = 0$).

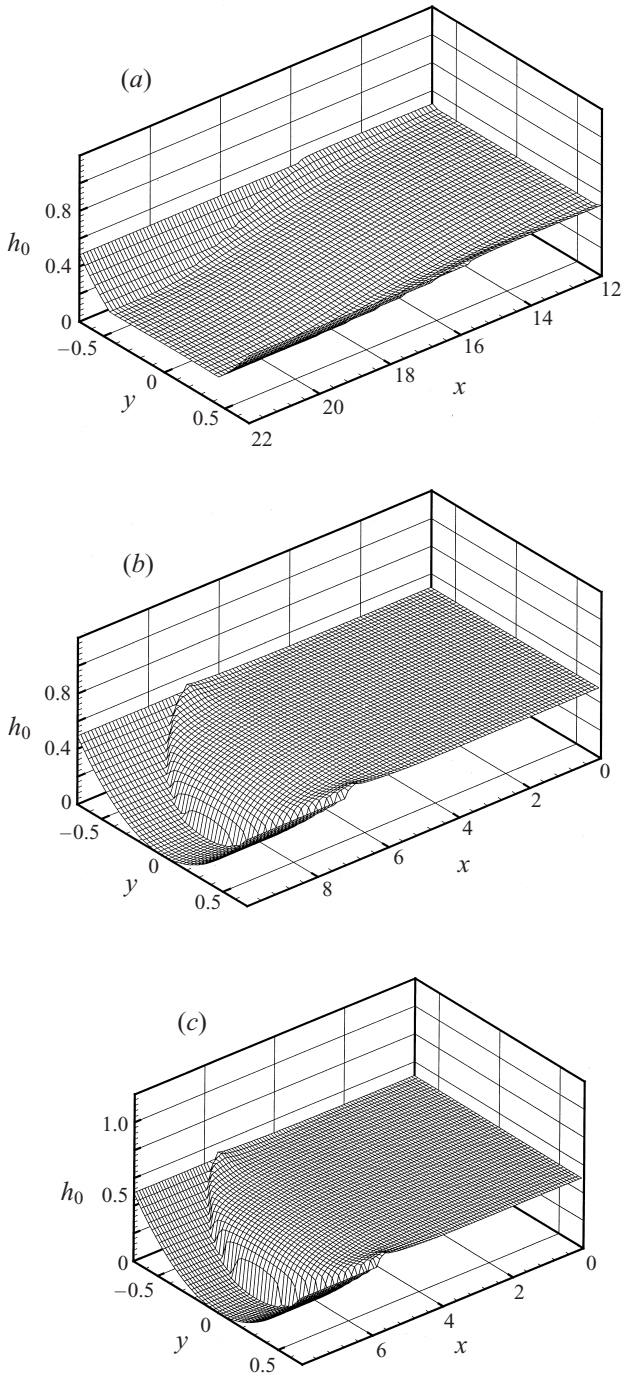

FIGURE 7. Yield surface of the wave front in a parabolic channel ($n = 2, m = 1, \alpha = 0.5$): (*a*) flowing downstream ($h_+ = 0.7$), (*b*) stagnant downstream ($h_+ = 0.3$), (*c*) dry downstream ($h_+ = 0$).

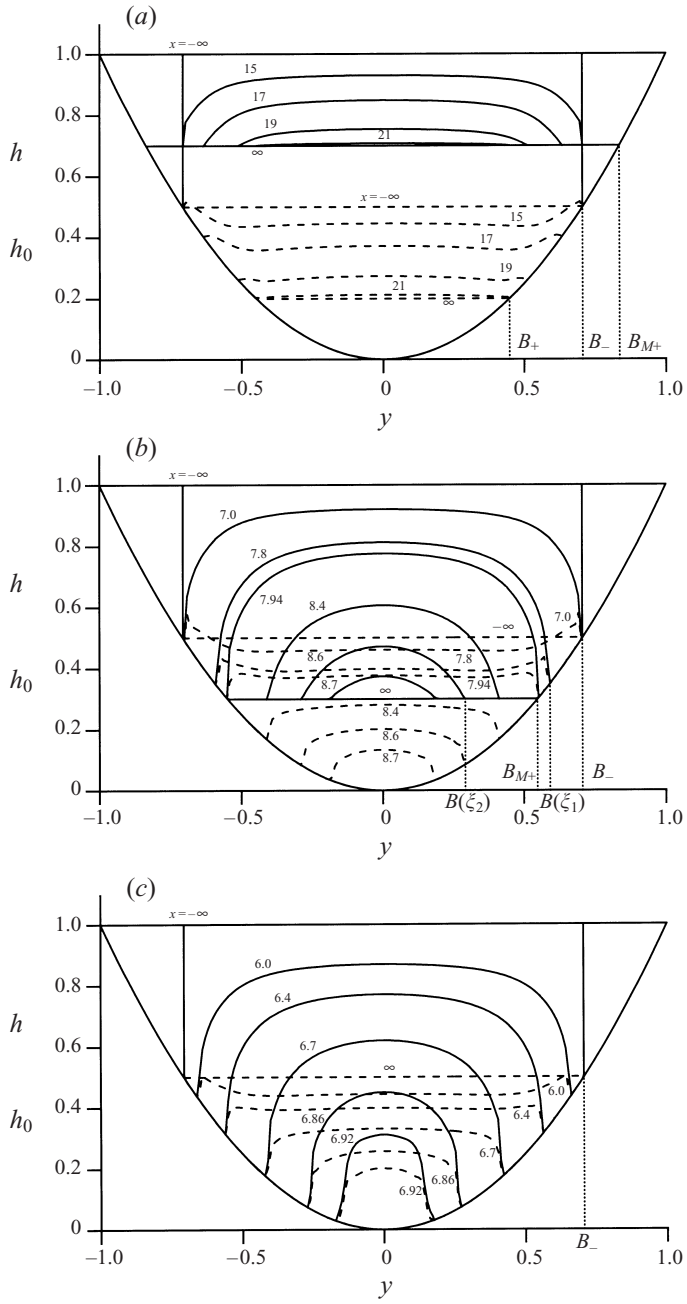

FIGURE 8. Cross-sectional profiles of the free surface and the yield surface of the stationary wave at several stations along a parabolic channel ($n = 2, m = 1, \alpha = 0.5$). The free surface is shown by solid lines and the yield surface by broken lines. The wave front is located at $x = 22.6$, 8.77 and 6.94 for (*a*), (*b*) and (*c*) respectively. (*a*) Flowing downstream ($h_+ = 0.7$), (*b*) stagnant downstream ($h_+ = 0.3$), (*c*) dry downstream ($h_+ = 0$).

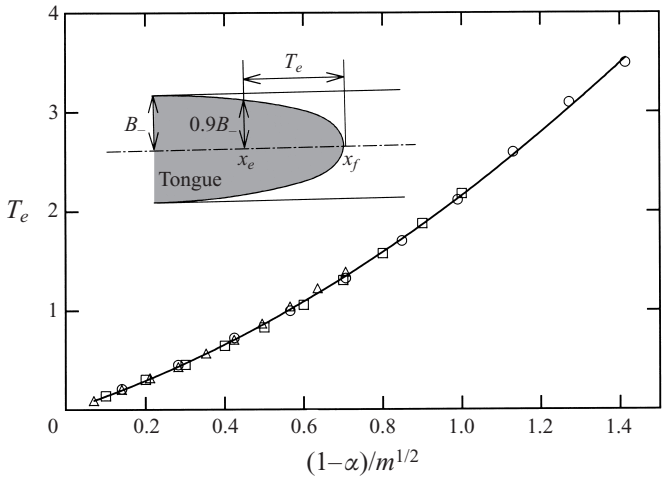

FIGURE 9. The effective length of tongue T_e as a function of $(1-\alpha)/m^{1/2}$: ○, $m = 0.5$; □, $m = 1.0$; △, $m = 2.0$; ——, equation (5.7).

To see more details, the cross-sectional views are shown at several x-stations in figure 8(a–c). Note that figures 8(a) and 8(b) also correspond to the cases where $B_{M+} > B_-$ (low influx) and $B_{M+} < B_-$ (high influx) respectively. When the downstream is flowing, the cross-section of the free surface is almost flat in the central region while h decreases monotonically with $|y|$ near the lateral edges. When the downstream is stagnant, i.e. when h_+ is smaller, h in the central region is more rounded and the slope of h near the lateral boundary of the flow edge becomes steep. These features are most pronounced in the dry bed case. Near the wave front, the yield surface height, h_0, decreases monotonically as $|y|$ increases. However, at the rear it first increases and then decreases as $|y|$ increases. This is a feature common to the flowing, stagnant and dry downstreams in figure 8. Note that if the half-width of the flow region is greater than the downstream half-width of the mud, i.e. $B > B_{M+}$, then the edge intersects the dry bed; $h = H$ at $y = B$ (see e.g. $B(\xi_1)$ in figure 8b). If on the other hand $B < B_{M+}$, the free surface height at the lateral edge of the flow region equals the initial free surface height; $h = h_+$ at $y = B$ (see e.g. $B(\xi_2)$ in figure 8b).

As a measure of the length of the tongue we first find the location x_e where the tongue width reaches 90% of B_-. This is calculated by numerically solving $B(x_e) = 0.9B_-$. The distance between x_e and the wave front on the centreline (x_f) is defined as the effective length of the tongue, T_e. From many calculations for the dry downstream the relation between the ratio T_e/B_- and the Bingham parameter α is found for several values of m. Typically as α increases, this ratio decreases almost linearly, and also becomes smaller for larger value of m. For the complete range of α, we can plot all the results on a single curve as shown in figure 9:

$$T_e = 0.835[(1-\alpha)/m^{1/2}]^2 + 1.33[(1-\alpha)/m^{1/2}], \tag{5.5}$$

implying that the dimensionless T_e is uniquely related to $(1-\alpha)/m^{1/2}$. For possible practical applications we return to dimensional parameters marked by asterisks,

$$T_e^* = T_e h_-^* \cot\theta, \quad m^* = m(h_-^*)^{-1} \tan^2\theta. \tag{5.6}$$

Equation (5.5) can be rewritten as

$$\frac{T_e^*}{h_-^* \cot\theta} = 0.835\left[\frac{(h_-^* - h_c^*)\tan\theta}{h_-^*(h_-^* m^*)^{1/2}}\right]^2 + 1.33\left[\frac{(h_-^* - h_c^*)\tan\theta}{h_-^*(h_-^* m^*)^{1/2}}\right] \tag{5.7}$$

where h_c^* is the critical depth defined by (2.17).

5.2. *The wave speed*

The propagation speed of a stationary wave is of course a result of the numerical solution at large time. As suggested by observations of the numerical results discussed in the previous section (cf. figure 8), the same result can be derived analytically for both wet and dry downstreams.

The wave profile and the phase speed of the stationary wave must satisfy (5.2). Along the centreline, there is no flux in the y-direction due to symmetry:

$$q_y = 0 \quad \text{at } y = 0. \tag{5.8}$$

At the local edges of the flow region, the fluxes in both the x- and y-directions must vanish:

$$q_x = q_y = 0 \quad \text{at } y = B(\xi) \tag{5.9}$$

where B is the half-width of the flow region. It follows by integrating (5.2) with respect to y from 0 to $B(\xi)$ that

$$\frac{\partial}{\partial\xi}\left[\int_0^B (-Ch + q_x)\mathrm{d}y\right] + Ch_B\frac{\mathrm{d}B}{\mathrm{d}\xi} = 0. \tag{5.10}$$

We now define the section-averaged free surface height $\langle h\rangle$ and flux $\langle q_x\rangle$ by

$$\langle h\rangle = \frac{1}{B}\int_0^B h\mathrm{d}y, \quad \langle q_x\rangle = \frac{1}{B}\int_0^B q_x\mathrm{d}y. \tag{5.11}$$

Equation (5.10) can then be rewritten as

$$\frac{\partial}{\partial\xi}\left[(-C\langle h\rangle + \langle q_x\rangle)B\right] + Ch_B\frac{\mathrm{d}B}{\mathrm{d}\xi} = 0. \tag{5.12}$$

Far upstream ($\xi \to -\infty$), the half-width of the flow region B_-, the total discharge, and the section-averaged flux, $\langle q_x\rangle_-$ can be expressed as functions of the upstream centreline depth h_- by setting $h_S = h_-$ in (3.5), (3.6) and (3.7), respectively.

Case (a): high influx rate ($h_+ < h_- - \alpha$)

(i) *Flowing downstream* ($h_+ > \alpha$). The flow half-width B_+ and $\langle q_x\rangle_+$ are obtained by setting $h_S = h_+$ in (3.5) and (3.7), respectively. Integration of (5.12) with respect to ξ from $-\infty$ to ∞ leads to

$$C = \frac{\langle q_x\rangle_- B_- - \langle q_x\rangle_+ B_+}{h_- B_- - h_+ B_+ + \displaystyle\int_{-\infty}^{\infty} h_B\frac{\mathrm{d}B}{\mathrm{d}\xi}\mathrm{d}\xi}. \tag{5.13}$$

In order to carry out the integration in (5.13), the value of h_B is needed. Referring to figure 5(*ai*), we let h_- be sufficiently large so that $B_- > B_{M+}$, or, equivalently $h_+ < h_- - \alpha$. As ξ increases from $-\infty$, the flow half-width $B(\xi)$ decreases from B_- monotonically until the wave front joins the uniform downstream ($B(\xi) = B_{M+}$) where the orgin of the ξ-coordinate is defined. For $\xi > 0$ the flow width continues to decrease to B_+. This means that ahead of the wave front the downstream side

is partially dry: the bed is dry for $B_{M+} < |y|$ and is wet for $0 \leqslant |y| \leqslant B_{M+}$. The numerical results obtained in the previous section show that, at the lateral edge of the wave front, the free surface intersects the bottom in the initially dry region (namely $h_B = H$, see $B(\xi_1)$ figure 8*b*) while the free surface height in the intially wet region equals h_+ (see $B(\xi_2)$ in figure 8*b*), i.e.

$$h(\xi, y = B(\xi)) = \begin{cases} H(B(\xi)) & \text{if } -\infty < \xi < 0 \ (B_{M+} \leqslant B(\xi) \leqslant B_-), \\ h_+ & \text{if } 0 < \xi < \infty \ (0 \leqslant B(\xi) \leqslant B_{M+}). \end{cases} \tag{5.14}$$

Using (5.14) the integral in (5.13) can be further reduced to

$$\int_{-\infty}^{\infty} h_B \frac{\mathrm{d}B}{\mathrm{d}\xi}\mathrm{d}\xi = \int_{-\infty}^{0} h_B \frac{\mathrm{d}B}{\mathrm{d}\xi}\mathrm{d}\xi + \int_{0}^{\infty} h_B \frac{\mathrm{d}B}{\mathrm{d}\xi}\mathrm{d}\xi = \frac{m}{n+1}\left[B_{M+}^{n+1} - B_-^{n+1}\right] + h_+(B_+ - B_{M+}). \tag{5.15}$$

Substitution of (5.15) into (5.13) yields

$$\begin{aligned} C &= \frac{\langle q_x\rangle_- B_- - \langle q_x\rangle_+ B_+}{h_- B_- - h_+ B_{M+} + [m/(n+1)]\left[B_{M+}^{n+1} - B_-^{n+1}\right]} \\ &= \frac{(n+1)\left[(h_- - \alpha)^{1/n}\langle q_x\rangle_- - (h_+ - \alpha)^{1/n}\langle q_x\rangle_+\right]}{(nh_- + \alpha)(h_- - \alpha)^{1/n} - nh_+ h_+^{1/n}}. \end{aligned} \tag{5.16}$$

(ii) *Stagnant downstream* ($h_+ < \alpha$). Since there is no flow far downstream, the phase speed can be derived by taking the limit of $B_+ = 0$ in (5.16)

$$\begin{aligned} C &= \frac{\langle q_x\rangle_- B_-}{h_- B_- - h_+ B_{M+} + [m/(n+1)]\left[B_{M+}^{n+1} - B_-^{n+1}\right]} \\ &= \frac{(n+1)(h_- - \alpha)^{1/n}\langle q_x\rangle_-}{(nh_- + \alpha)(h_- - \alpha)^{1/n} - nh_+ h_+^{1/n}}. \end{aligned} \tag{5.17}$$

In the limit where the downstream bed is completely dry, i.e. $h_+ = 0$ and $B_{M+} = 0$, (5.17) is reduced to

$$C_{dry} = \frac{\langle q_x\rangle_- B_-}{h_- B_- - [m/(n+1)]B_-^{n+1}} = \frac{(n+1)\langle q_x\rangle_-}{(nh_- + \alpha)}. \tag{5.18}$$

In this case, the section-averaged velocity at far upstream can be described as

$$\langle u\rangle_- = \frac{\langle q_x\rangle_-}{\dfrac{1}{B_-}\displaystyle\int_0^{B_-}(h_- - H)\mathrm{d}y} = \frac{(n+1)\langle q_x\rangle_-}{(nh_- + \alpha)} \tag{5.19}$$

which is the same as the phase velocity of the stationary wave, as is expected by mass conservation.

Case (*b*)*: low influx rate* ($h_+ > h_- - \alpha$)

(i) *Flowing downstream* ($h_+ > \alpha$). Referring to figure 5(*b*i), we consider the case where the upstream flow region is not too wide so that $B_{M+} > B_- > B_+$ or equivalently, $h_+ > h_- - \alpha$; then the bed is everywhere wet ahead of the wave front. Consequently $h_B = h_+$ throughout the transition region so that

$$\int_{-\infty}^{\infty} h_B \frac{\mathrm{d}L}{\mathrm{d}\xi}\mathrm{d}\xi = h_+(B_+ - B_-). \tag{5.20}$$

Substitution of (5.20) into (5.13) leads to

$$C = \frac{\langle q_x\rangle_- B_- - \langle q_x\rangle_+ B_+}{B_-(h_- - h_+)}$$

$$= \frac{(h_- - \alpha)^{1/n}\langle q_x\rangle_- - (h_+ - \alpha)^{1/n}\langle q_x\rangle_+}{(h_- - h_+)(h_- - \alpha)^{1/n}}. \tag{5.21}$$

(ii) *Stagnant downstream* ($h_+ < \alpha$). Referring to figure 5(*b*ii), we obtain the phase speed by setting $B_+ = 0$ in (5.21):

$$C = \frac{\langle q_x\rangle_-}{h_- - h_+}. \tag{5.22}$$

Note that in all the cases described above the phase speed is a function of α, h_-, h_+, and n, but is independent of m.

Let us examine some limiting cases. The Newtonian limit is found by setting $\alpha = 0$ in (5.16):

$$C_N = \frac{2n^2\left[h_-^{3n+1/n} - h_+^{3n+1/n}\right]}{(2n+1)(3n+1)\left[h_-^{n+1/n} - h_+^{n+1/n}\right]}. \tag{5.23}$$

The two-dimensional limit of a flat bed can be obtained by setting $n \to \infty$ in (5.16), (5.17), (5.21), and (5.22). For a flowing downstream the phase speed becomes

$$C_{2D} = \tfrac{1}{6}\left[2(h_-^2 + h_-h_+ + h_+^2) - 3\alpha(h_- + h_+)\right], \tag{5.24}$$

while for a stagnant downstream it is reduced to

$$C_{2D} = \frac{(h_- - \alpha)^2(2h_- + \alpha)}{6(h_- - h_+)}. \tag{5.25}$$

These limiting results agree with those by Liu & Mei (1989). If we further take the Newtonian limit of (5.24) and (5.25), then

$$C_{2D,N} = \tfrac{1}{3}(h_-^2 + h_-h_+ + h_+^2), \tag{5.26}$$

and

$$C_{2D,N} = \frac{h_-^3}{3(h_- - h_+)} \tag{5.27}$$

respectively, as was given by Mei (1966).

The relation between C and α is plotted in figure 10 for $h_- = 1$ and $n = 2$, and for various values of h_+. Note that the phase speed does not depend on m. The parametric domains of the four subcases are separated by the two dashed curves $h_+ = \alpha$ and $h_+ = h_- - \alpha = 1 - \alpha$ in the figure. Results for the flowing downstream lie above the curve $h_+ = \alpha$, and those for the stagnant downstreams, below. Results for high influx rates lie below the curve $h_+ = 1 - \alpha$, and those for low influx rates, above. It is clear that the phase speed decreases with the increase of α and that the phase speed increases as h_+ increases.

The analytically predicted phase velocities for various cases are confirmed by the numerical results from transient computations, as shown by dots in figure 10. To compare the effects of channel cross-sections the phase speed of a mud wave down a dry bed is plotted in figure 11 for all α and for $n = 1, 2, 3$. The corresponding result for a plane bed (i.e. uniform wave in the y-direction) is also included. As n increases,

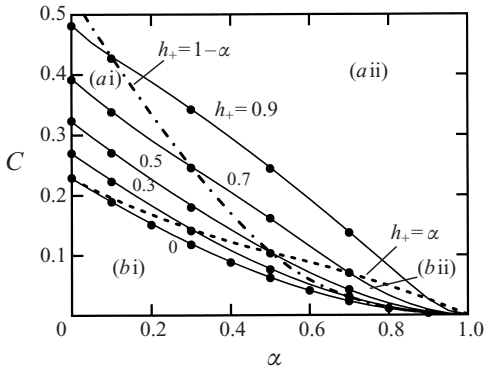

FIGURE 10. Phase speed of the stationary wave in a parabolic channel as a function of α and h_+. Solid line: analytical, closed circle: numerical.

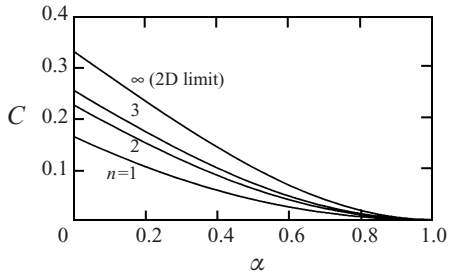

FIGURE 11. Phase speed of the stationary wave in a dry channel of cross-section $H = m|y|^n$ as a function of α and n.

the phase speed increases, and attains the two-dimensional value when $n \to \infty$ as described in (5.27). Similar confirmations have also been obtained for triangular and semi-elliptic channels, not presented here.

6. Transient spreading after dam collapse

Consider a parabolic channel ($n = 2$) with a mud reservoir to the left ($x < 0$) of a dam at $x = 0$. Initially the mud in the reservoir is at rest and occupies a finite length of the channel so that the free surface height is described by

$$h(x,t) = 1 + x, \quad my^2 - 1 \leqslant x \leqslant 0, \qquad t < 0. \tag{6.1}$$

Elsewhere ($x > 0$ and $x < my^2 - 1$), the bed is initially dry. Note that the initial normalized slope of the free surface in the reservoir is unity, $\partial h/\partial x = 1$, in the present coordinate system; in physical coordinates the corresponding free surface is horizontal. At $t = 0$ the dam disappears and the reservoir mud is released suddenly, and moves downstream until the final state of static equilibrium.

Calculations are made for three parabolic channels with different bank steepnesses $m = 0.5, 1, 2$, and different mud plasticities $\alpha = 0.2$ to 0.9. The numerical domain is large enough so that the fluid edges are far from the numerical boundary at all times. On the centreplane ($y = 0$), symmetry is assumed. The typical grid size used in the calculations is $\Delta x = 0.025$, $\Delta y = 0.025$, and $\Delta t = 0.01$. In general, a very long time,

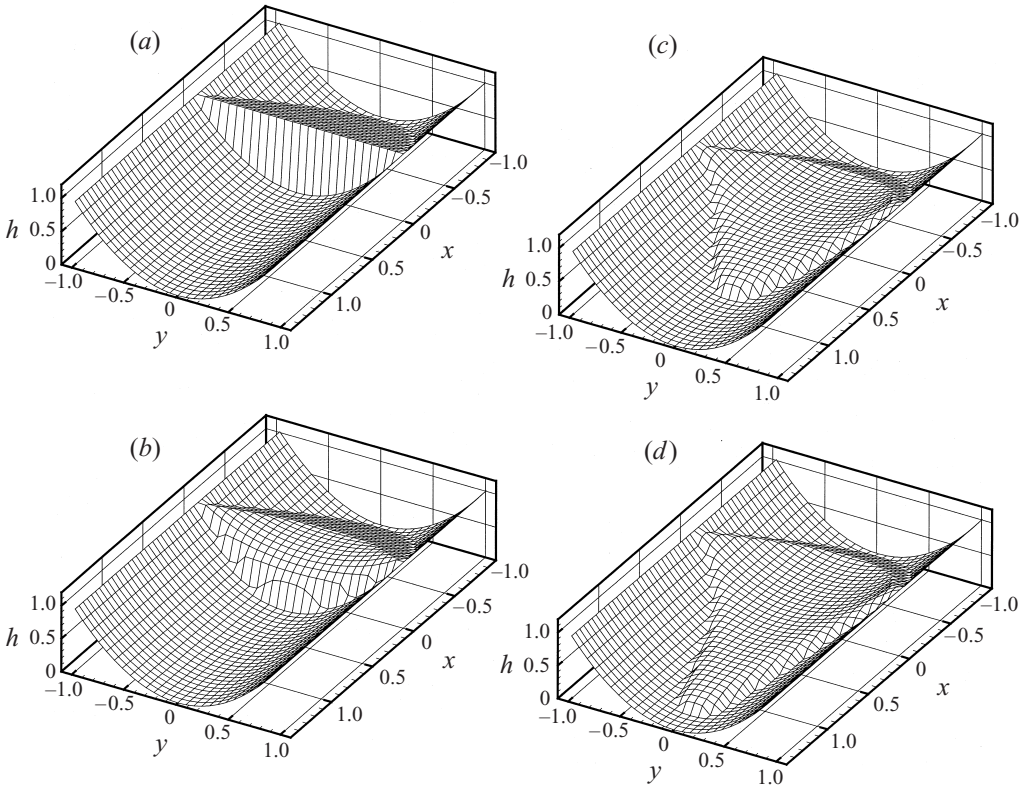

FIGURE 12. Sample evolution of the free surface after dam break. (*a*) $t = 0$, (*b*) $t = 5$, (*c*) $t = 50$, (*d*) $t = 10\,000$ ($\alpha = 0.3, n = 2, m = 1$).

from $O(10^3)$ to $O(10^5)$, is necessary to reach the final stage. This relaxation time, t_R, increases as α decreases or as m increases. The increase of t_R is quite significant for $\alpha < 0.4$. For $\alpha = 0.2$ and $m > 0$, we terminated the calculation before the final stage is attained. The final front locations for these cases are deduced by using the Domb–Sykes extrapolation technique.

Typical evolutions of the free surface are displayed in figure 12 for $\alpha = 0.3$ and $m = 1$. Just after the dam break, the movement of the fluid is significant. The front spreads downstream and forms a fan. The free surface is convex upward in the front part and concave upward in the rear. Thus fluid is emptied from the rear to fill the advancing front. The central part of the front elongates gradually and forms a tongue.

For sufficiently large t, the fluid pile comes to rest. At this final stage of deposition, h must satisfy the condition of static equilibrium

$$(h - H)\left[\left(1 - \frac{\partial h}{\partial x}\right)^2 + \left(\frac{\partial h}{\partial y}\right)^2\right]^{1/2} = \alpha \tag{6.2}$$

according to (2.19). Along the centreline, this condition can be further reduced to

$$h\left|1 - \frac{\partial h}{\partial x}\right| = \alpha \tag{6.3}$$

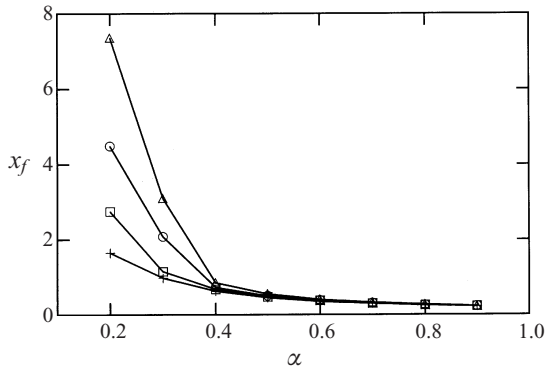

FIGURE 13. Final location of the mud front as a function of α and m: +, $m = 0$; □, $m = 0.5$; ○, $m = 1.0$; △, $m = 2.0$.

due to symmetry. This equation also governs the front and the back of a two-dimensional mud pile at the end of downward flow and can be integrated to give

$$x - x_o = h - h_o + \alpha \ln \frac{|h - \alpha|}{|h_o - \alpha|} \quad \text{where } \frac{\partial h}{\partial x} < 1 \text{ (the front)} \tag{6.4}$$

and

$$x_o - x = h_o - h - \alpha \ln \frac{h_o + \alpha}{h + \alpha} \quad \text{where } \frac{\partial h}{\partial x} > 1 \text{ (the back)} \tag{6.5}$$

where $h = h_o$ at $x = x_o$ (Liu & Mei 1989). For two-dimensional problems, the values of x_o and h_o can be determined from the initial mud volume by mass conservation. For the three-dimensional problem here, x_o and h_o are coupled to the flow off the centreplane and can only be solved as a part of the initial value problem involving x, y and t. The result depends not only on the total fluid mass but also on the initial shape of the pile as well as the channel geometry.

In figure 13, the final location of the mud front along the centreline, x_f, is plotted as a function of α for three values of m. The limiting result corresponding to an infinitely wide channel ($m = 0$) is also included for comparison. Note that the final extent of deposition increases as m increases, thus the front spreads farther in a channel with steeper banks, which urge more fluid towards the channel axis to form a narrower and faster tongue. The effect of m on x_f becomes very strong for small values of α (more Newtonian).

As expected, the final extent also increases as the plasticity measure α decreases. In the Newtonian limit where $\alpha = 0$, the fluid spreads out indefinitely.

7. Summary remarks

On the basis of the long-wave approximation, a theory has been developed for the slow flow of a Bingham fluid in an inclined channel of finite width. For steady uniform flows, the velocity distribution, total discharge, and section-averaged flux are found analytically in terms of the fluid property and the channel geometry. Typically the cross-section consists of three zones: around the centreplane of the channel there is a shear zone at the bottom and a plug flow zone at the top, separated by the yield surface. In addition there are two calm zones near the banks. At

the interface of the stagnant zone and the flowing zone, the fluid velocity vanishes. The final geometry of the stationary wave front due to the steady supply of mud far upstream has been calculated numerically by solving an initial-boundary-value problem with a free boundary. The dependence on the initial flow depth, bottom geometry, and the fluid property has been investigated. For both wet and dry downstreams, analytical expressions for the phase speed have been derived. Finally, we have studied the sudden release of fluid mud due to the sudden breaking of a dam. The transient spreading of mud is simulated numerically from the release to its final stoppage. The relation between the final extent of mud and fluid property is also predicted.

The mathematical and numerical model developed here can be applied straightforwardly to slow flows on an unbounded incline with slowly varying terain. For simulating a wider variety of fluids and range of shearing rates, modifications of Herschel–Bulkley models are desirable and are not difficult. A more challenging task is to treat a channel whose width and depth are comparable. In addition, the dynamics of fast flows and the formation of roll waves in a shallow channel of finite width, where the fronts of roll waves must be curved, is worthy of investigation.

C.C.M. acknowledges the support of Office of Naval Research (Grant N00014-89-J-3128) and US National Science Foundation (Grants CTS 9634120 adn CTS 0075713). M.Y.'s one-year visit to MIT was supported by Kanazawa University, Japan.

Appendix A. Linearized instability of sinusoidal waves

Let a small perturbation be added to the uniform flow as

$$h = h_S + \bar{h}, \quad h_0 = h_{0S} + \bar{h}_0 = h_S - \alpha + \bar{h}_0. \tag{A 1}$$

Consider periodic waves for disturbances

$$(\bar{h}, \bar{h}_0) = (h'(y), h_0'(y))\mathrm{e}^{\mathrm{i}(kx-\omega t)}, \tag{A 2}$$

where k is the real wavenumber, and $\omega = \omega_r + \mathrm{i}\omega_i$ is complex. From the linearized equations, an eigenvalue condition for non-trivial solutions of h' is obtained as

$$\frac{\mathrm{d}}{\mathrm{d}y}\left[\frac{(2d_S+\alpha)(d_S-\alpha)^2}{6}\frac{\mathrm{d}h'}{\mathrm{d}y}\right] + h'\left[\mathrm{i}(\omega_r - kd_S(d_S-\alpha)) - \omega_i - \frac{k^2}{3}(d_S^3-\alpha^3)\right] = 0 \tag{A 3}$$

with the boundary conditions

$$h' = \text{finite} \quad \text{at } y = B, \tag{A 4a}$$

$$\frac{\mathrm{d}h'}{\mathrm{d}y} = 0 \quad \text{at } y = 0, \tag{A 4b}$$

where d_S is the local fluid depth in steady uniform flow, which is defined as

$$d_S(y) = h_S - H(y). \tag{A 5}$$

We multiply h'^*, the complex conjugate of h', by (A 3) and then integrate the product equation with respect to y from $y = 0$ to $y = B$. Using $d_S - \alpha = 0$ on $y = B$,

we obtain

$$\omega_r = \frac{\displaystyle\int_0^B k d_S (d_S - \alpha)|h'|^2 \mathrm{d}y}{\displaystyle\int_0^B |h'|^2 \mathrm{d}y} > 0, \tag{A 6a}$$

$$\omega_i = -\frac{\displaystyle\int_0^B \frac{(2d_S + \alpha)(d_S - \alpha)^2}{6} \left|\frac{\mathrm{d}h'}{\mathrm{d}y}\right|^2 \mathrm{d}y + k^2 \int_0^B \frac{(d_S^3 - \alpha^3)}{3} |h'|^2 \mathrm{d}y}{\displaystyle\int_0^B |h'|^2 \mathrm{d}y} < 0. \tag{A 6b}$$

These results show that the flow is unconditionally stable for small disturbances. The one-dimensional limit of these equations are

$$\omega_r = k h_S (h_S - \alpha) > 0, \quad \omega_i = -\tfrac{1}{3} k^2 (h_S^3 - \alpha^3) < 0. \tag{A 7a, b}$$

Appendix B. Uniform flow in an elliptic channel

The channel cross-section is described by

$$\frac{y^2}{a^2} + \frac{H(y)^2}{b^2} = 1 \ (-b \leqslant H(y) \leqslant 0, -a \leqslant y \leqslant a) \tag{B 1}$$

or equivalently,

$$y = a \sin\phi, \quad H(y) = -b \cos\phi \ (-\pi/2 \leqslant \phi \leqslant \pi/2), \tag{B 2}$$

in which ϕ is taken counter-clockwise from the negative direction of the z-axis. The half-width of the flow region, B, is determined from (3.1) as

$$B = \frac{a}{b} \left[b^2 - (h_S - \alpha)^2\right]^{1/2} = a \sin\phi_B. \tag{B 3}$$

The total discharge Q is

$$Q = 2a \sin\phi_B [e_1 + e_2 \cos\phi_B + e_3 \cos^2\phi_B + e_4 \cos^3\phi_B] + 2a e_2 \phi_B \tag{B 4}$$

where the coefficients e_i $(i = 1, 4)$ are given in terms of h_S and b as

$$e_1 = -\tfrac{1}{6} \left[(h_S - \alpha)^3 - 3h_S(h_S - \alpha)^2 - 2b^2(h_S - \alpha) - 2b^2 h_S\right], \tag{B 5a}$$

$$e_2 = \tfrac{1}{8} b \left[4h_S(h_S - \alpha) + b^2\right], \quad e_3 = \tfrac{1}{6} b^2 (2h_S - \alpha), \quad e_4 = \tfrac{1}{12} b^3. \tag{B 5b–d}$$

The total discharge Q is proportional to a. The section-averaged flux $\langle q_x \rangle$ becomes

$$\langle q_x \rangle = [e_1 + e_2 \cos\phi_B + e_3 \cos^2\phi_B + e_4 \cos^3\phi_B] + \frac{e_2 \phi_B}{\sin\phi_B}. \tag{B 6}$$

The section-averaged flux is a function of α and b but is independent of a. The numerical results are qualitatively similar to those for the parabolic channel and are not plotted.

REFERENCES

ALLERSMA, E. 1980 Mud in estuaries and along coasts. In *Proc. Intl Symp. River Sedimentation, Beijing, China* (ed. N. Qian), pp. 663–685. Guanhua Press.

Balmforth N. J., Burbidge, A. S., Craster, R. V., Salzig, J. & Shen, A. 2000 Visco-plastic models of isothermal lava domes. *J. Fluid Mech.* **403**, 37–65.

Balmforth, N. J. & Craster, R. V. 1999 A consistent thin-layer theory for Bingham plastics. *J. Non-Newtonian Fluid Mech.* **84**, 65–81.

Bird, R. B., Dai, G. C. & Yarusso, B. J. 1983 The rheology and flow of viscoplastic materials. *Rev. Chem. Engng* **1**, 1–70.

Coussot, P. 1997 *Mudflow Rheology and Dynamics*. IAHR/AIRH Monograph.

Coussot, P. & Proust, S. 1996 Slow, unconfined spreading of a mudflow. *J. Geophys. Res.* **101**, 25217–25229.

Coussot, P., Proust, S. & Ancey, C. 1996 Rheological interpretation of deposits of yield stress fluids. *J. Non-Newtonian Fluid Mech.* **66**, 55–70.

Crochet, M. J., Davies, A. U. & Walters, K. 1984 *Numerical Simulation of Non-Newtonian Fluid Mechanics*. Elsevier.

Crochet, M. H. J. & Walters, K. 1983 *Numerical methods in non-Newtonian fluid mechanics. Ann. Rev. Fluid Mech.* **15**, 241–260.

Douglas, J. J. 1955 On the numerical integration of $\partial^2 u/\partial x^2 + \partial^2 u/\partial y^2 = \partial u/\partial t$ by implicit methods. *J. Soc. Indust. Appl. Maths* **3**, 42–65.

Huang, X. & Garcia, M. H. 1998 A Herschel–Bulkley model for mud flow down a slope. *J. Fluid Mech.* **374**, 305–333.

Hulme, G. 1974 The interpretation of lava flow morphology. *Geophys. J. R. Astrophys. Soc.* **39**, 361–383.

Johnson, A. M. 1970 *Physical Processes in Geology*. Freeman, Cooper & Company.

Johnson, A. M. & Rodine, J. R. 1984 Debris flow. In *Slope Instability* (ed. D. Brunsden & D. B. Prior), Chap. 8. John Wiley & Sons.

Keunings, R. 1990 Progress and challenges in computational rheology. *Rheologica Acta* **29**, 556–570.

Krone, R. B. 1963 A study of rheological properties of estuarial sediments. *Ser. Rep.* 63-8. Hydraulic Engineering Laboratory and Sanitary Research Laboratory, University of California, Berkeley.

Liu, K. F. & Mei, C. C. 1989 Slow spreading of a sheet of Bingham fluid on an inclined plane. *J. Fluid Mech.* **207**, 505–529.

Liu, K. F. & Mei, C. C. 1990 Approximate equations for the slow spreading of a thin sheet of Bingham plastic fluid. *Phys. Fluids* A **2**, 30–36.

Liu, K. F. & Mei, C. C. 1994 Roll waves on a layer of a muddy fluid down a gentle slope – A Bingham model. *Phys. Fluids* **6**, 2577–2590.

McDowell, B. & Raymer, S. 1986 Eruption in Columbia. *National Geographic* **169**, 640–653.

Mao, W. & Khayat, R. E. 1995 Numerical simulation of transient planar flow of a viscoelastic material with two moving free surfaces. *Intl J. Numer. Meth. Fluids* **21**, 1137–1151.

Mei, C. C. 1966 Nonlinear gravity waves in a thin sheet of viscous fluid. *J. Maths. Phys.* **45**, 266–288.

Migniot, P. C. 1968 Étude de propriétés physiques de différents sediments tres fins et de leur comportment sous des action hydrodynamiques. *La Houille Blanche* **7**, 591–620.

Mileti, D. S., Bolton, P. A., Fernandez, G. & Updike, R. G. 1991 *The Eruption of Nevado Del Ruiz Volcano, Colombia, South America*. National Academy Press, Washington DC.

Newhall, C. G. & Punongbayan, R. S. 1996 *Fire and Mud, Eruptions and Lahars of Mount Pinatubo, Phillipines*. University of Washington Press.

Ng, C. & Mei, C. C. 1994 Roll waves on a shallow layer of mud modeled as a power-law fluid. *J. Fluid Mech.* **263**, 151–183.

Peaceman, D. W. & Rachford, H. H. 1955 The numerical solution of parabolic and elliptic differential equations. *J. Soc. Indust. Appl. Maths* **3**, 28–41.

Petera, J. & Nassehi, V. 1996 Finite element modelling of free surface viscoelastic flows with particular application to rubber mixing. *Intl J. Numer. Meth. Fluids* **23**, 1117–1132.

Piau, J. M. 1996 Flow of a yield stress fluid in a long domain. Application to flow on an inclined plane. *J. Rheology* **40**, 711–723.

Prager, W. 1961 *Introduction to Mechanics of Continua*. Ginn and Company.

Qian, Y., Yang, W., Zhao, W., Cheng, X. & Zhang, L. 1985 Experimental study on homogeneous hyperconcentrated flow. In *Proc. Intl Workshop on Flow at Hyperconcentrations of Sediment, Beijing, China* (ed. N. Qian), vol. ii.1, pp. 1–13. IRTCES.

Sato, T. & Richardson, S. M. 1994 Numerical simulation method for viscoplastic flows with free surfaces – fringe element generation method. *Intl J. Numer. Meth. Fluids* **19**, 555–574.

Taylor, A. J. & Wilson, S. D. R. 1997 Conduit flow of an incompressible, yield-stress fluid. *J. Rheology* **41**, 93–101.

Wang, Z. & Qian, Y. 1985 A preliminary investigation on the mechanism of hyperconcentrated flow. In *Proc. Intl Workshop on Flow at Hyperconcentrations of Sediment, Beijing, China* (ed. N. Qian), vol. ii.4, pp. 1–13. IRTCES.

Wilson, S. D. R. & Burgess, S. L. 1998 The steady, spreading flow of a rivulet of mud. *J. Non-Newtonian Fluid Mech.* **79**, 77–85.

Wilson, S. D. R. & Taylor, A. J. 1996 The channel entry problem for a yield stress fluid. *J. Non-Newtonian Fluid Mech.* **65**, 165–176.